Elucidation of pore connection mechanism during ductile fracture of sintered pure iron by applying persistent homology to 4D images of pores: Role of open pore

Ando, Isshin
Department of Materials Science and Engineering, Kyushu University

Mugita, Yasutaka
Department of Materials Science and Engineering, Kyushu University

Hirayama, Kyosuke
Department of Materials Science and Engineering, Kyoto University

Munetoh, Shinji
Department of Materials Science and Engineering, Kyushu University

他

出版情報：Materials Science and Engineering: A. 828, pp.142112-, 2021-11-02. Elsevier
バージョン：
権利関係：

Elucidation of pore connection mechanism during ductile fracture of sintered pure iron by applying persistent homology to 4D images of pores: Role of open pore

Isshin Ando[a], Yasutaka Mugita[a], Kyosuke Hirayama[b], Shinji Munetoh[a], Masatoshi Aramaki[a], Fei Jiang[c], Takeshi Tsuji[d], Akihisa Takeuchi[e], Masayuki Uesugi[e] and Yukiko Ozaki[a]*

[a] Department of Materials Science and Engineering, Kyushu University, 744, Motooka, Nishi-ku, Fukuoka 819-0395, Japan

[b] Department of Materials Science and Engineering, Kyoto University, Yoshida-honmachi, Sakyo-ku, Kyoto 606-8501, Japan

[c] Department of Mechanical Engineering, Yamaguchi University, 12-16-1, Tokiwadai, Ube, Yamaguchi 755-8611, Japan

[d] Department of Earth Resources Engineering, Kyushu University, 744, Motooka, Nishi-ku, Fukuoka 819-0395, Japan

[e] Japan Synchrotron Radiation Research Institute (JASRI), 1-1-1, Kouto, Sayo-cho, Sayo-gun, Hyogo 679-5198, Japan

*Corresponding author: Yukiko Ozaki

Department of Materials Science and Engineering, Kyushu University

744, Motooka, Nishi-ku, Fukuoka 819-0395, Japan

Phone: +81-92-802-2941

Fax: +81-92-802-2990

E-mail: ozaki@zaiko.kyushu-u.ac.jp

Abstract

4D pore configurations including an open pore were visualized by synchrotron X-ray laminography during the ductile fracturing process and then interpreted quantitatively using persistent homology (PH), a topological measure. In particular, this study used the zeroth PH, where the radius of an equivalent volume sphere for each pore and the distances to the other pores can be estimated for pairs of pores. The pore configurations were quantified as a set of birth and death values $\{(b_i, d_i)\}$ and changes due to increasing strain were tracked. As a result, the zeroth PH revealed the following information at the final stage before fracturing. First, the pair configurations between the open pore and closed pores decreased owing to the adsorption of closed pores by the open pore. Second, the configuration between the elongated closed pore and the open pore, where equivalent volume spheres are overwrapped, increased. These configurational changes in pores predict the pore connection between the open pore and surrounding closed pores that eventually generates a ductile crack perpendicular to the tensile stress. This study demonstrated the effective interpretation of the pore connection process that is essential to ductile crack generation.

Keywords: ductile fracture, sintered iron, open pore, closed pore, persistent homology

1. Introduction

Powder metallurgical (PM) automobile parts must be downsized to achieve zero emissions. Toward this end, high-density compaction processes [1,2] such as double press double sintering (DPDS) and warm compaction (WC) are currently available. However, such high-density PM materials still contain pores, and therefore, their mechanical properties are not comparable to those of wrought steel [3]. The effects of such pores on crack initiation must be clarified to improve the reliability of PM materials for use as structural members. In recent years, several studies have investigated the fracture mechanisms and crack morphologies of fractured PM steels [4-10]. Torralba et al. conducted in-situ observations under loads using a scanning electron microscope (SEM) with a digital image correlation technique and found that initial cracks were generated from sharp pores with a high aspect ratio or in the area where Kirkendall pores formed in heterogeneous diffusion alloyed Fe–Ni–Cu–Mo–C steel propagated immediately to neighbouring pores in the sintered metallic steels [8]. Dudrová and Kabátová systematically reviewed the fractography of sintered Fe-Cu-C, Fe- 1.8% Cr and 4% Ni diffusion-bonded alloyed steel [9,10]. Nonetheless, proposing a suitable theoretical model for PM materials in a manner similar to those proposed for bulk materials [11-13] remains difficult because the sintered bodies contain hundreds of thousands of micropores or microcracks.

High-intensity X-ray computation tomography (CT) has used for observing microvoid initiation under a tensile load in wrought metals. Toda et al. conducted X-ray microtomography at Spring-8 to visualize the crack extending process under tensile loads between coarse micropores as snapshots for Al-based alloys containing Zn or Mg [14-19]. Furukimi et al. used a 4D technique with tensile tests and found that micropores around grain boundaries coalesced into cracks owing to the strain concentrations in industrial pure-iron sheets [20]. Chawla et al. first applied a 3D-CT technique to unloaded sintered metals and

then visualized the local stress concentration between pores using finite element models under tensile loads based on the pore configuration obtained from the 3D-CT images [21-24]. However, secondary initiated microvoids have not yet been tracked.

The authors have previously used synchrotron X-ray laminography to clarify the change process of pore configurations in sintered pure iron during a tensile test and demonstrated the applicability of persistent homology (PH), a type of topological analysis, to extract the configuration for < 3000 closed pores during the crack initiation stage within the confined area of a roughly 100-μm-thick slice without open pores [25]. In the present study, we investigated the role of open pores independently of that of closed pores by focusing on the mathematical connections between pores using PH. For this purpose, we considered more than 10^5 pores.

2. Experimental

2.1. Materials and specimen preparation for tensile test

The tensile test was conducted using a sintered pure iron powder specimen (JFE Steel Co., JIP301A) that was prepared as reported previously [25]. The specimen porosity was 11.7%, and it included open and closed pores as determined using Archimedes' water immersion technique. Further, it had dimensions of 2 mm (width), 1 mm (thickness), and 3 mm (length) in the centre area, and it was machined using a wire electric discharge machine.

2.2. In-situ 4D observation during tensile test by synchrotron X-ray laminography

High-resolution X-ray laminography experiments were performed at the BL20XU X-ray imaging beamline at SPring-8, where the maximum spatial resolution for volume reconstruction was around 1 μm and the minimum voxel size was as low as 0.3 μm [26-28]. The photon energy of the monochromatic X-ray beam generated by the liquid-nitrogen-

cooled Si (111) double-crystal monochromator was 37.7 keV. The specimen was placed on a rotatable stage, and the rotation axis was inclined at 45° to the X-ray beam. The detector was placed 18.0 mm from the centre of rotation on the specimen surface. A radiograph with a diameter of 1000 μm was taken about the centre area of the specimen with an exposure time of 300 ms at every 0.1° during a rotation. The captured images were reconstructed with isotropic voxels having a size of 0.5 μm from a series of radiographs by the filtered back projection algorithm and visualized as 3D images using the image-analysis software Avizo 9.1.1 (FEI Co.).

The laminography scans were performed before the tensile test at five distinct plastic deformations at every moment when the tensile test was interrupted and the load, applied at a constant strain rate of 10^{-3} s^{-1}, was discharged.

2.3. Analysis of connection between pores by PH

PH is a topological measure that quantifies point cloud configurations as 2D values [29]. In this method, the radius r of a sphere that is virtually placed at each point is increased from 0. As r increases, holes formed by the contact or overlap of spheres at specific points are created or disappear. Two radii—birth value b at the time when a hole surrounded by the spheres is generated and death value d when the hole disappears—are used. The persistent pair (b, d) corresponds to the point cloud configuration. As a result, the finite set of persistent pairs for n point cloud configurations, $\sum_{i=1}^{n}\{(b_i, d_i)\}$, can be plotted on the (x, y)-plane to produce the persistence diagram (PD). In 3D space, PD is defined from the zeroth to the second PD, that is, PD0, PD1 and PD2; these are respectively the configurations for two-point connections, more than three-points connections forming polygons, and more than four-points forming polyhedrons. A void-connection model has been proposed for the ductile fracture of metallic materials. Therefore, in this study, the remaining pores and microvoids

were considered point clouds, and the zeroth PD was applied to quantitatively analyse their connection process.

The zeroth PH for the pore group in sintered materials is as follows. Figs. 1a and 1b (left) illustrate the process of obtaining PD0 about a pair of a randomly selected i-th sphere pore and its adjacent pore. In the initial state, a sphere with an equivalent volume is placed at the barycentre of each pore. Then, these spheres are expanded or shrunk depending on whether they overlap (Case I or II). b_i is defined as the reverse-signed initial radius r_{i0} of the i-th sphere on the left. The pair (b_i, d_i) of two spheres is defined as follows:

$$b_i \equiv -r_{i0}\ (<0), \quad (1)$$

$$d_i \equiv sgn\ (\Delta) \times \sqrt{|\Delta|}, \quad (2)$$

$$\Delta \equiv r_{if}^2 - r_{i0}^2. \quad (3)$$

In Eq. 3, r_{if} is the radius of the i-th sphere at contact. $sgn\ (\Delta)$ is negative in Case II where two spheres with equivalent volumes overlap as for neighboring pores with high aspect ratio. As shown in Figs. 1a and 1b for the final case at contact, a death value d_i, which indicates the length of a generatrix line formed by the initial sphere and the contacting point at the final stage, corresponds to the distance between the sphere of interest and the adjacent sphere in both cases. Because the pair cloud $\{(b_i, d_i)\}$ in Cases I and II is respectively in the second and third quadrants, these cases can be easily distinguished on the (x, y)-plane.

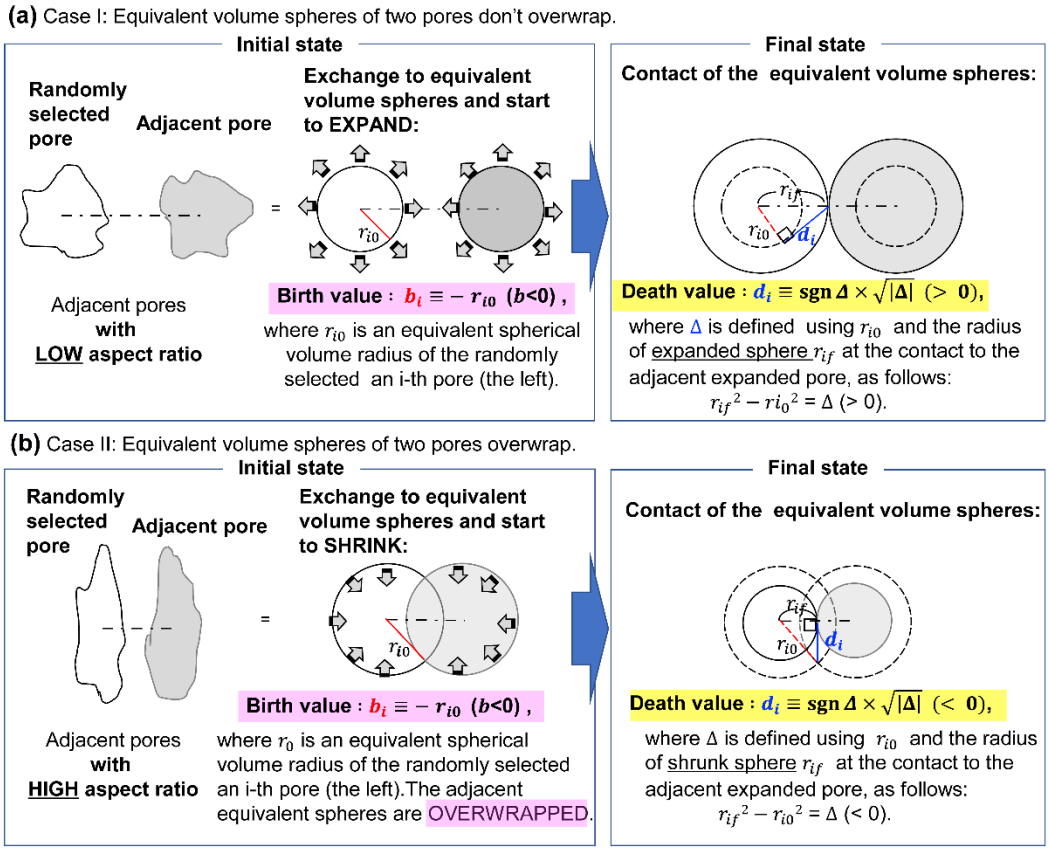

Fig. 1. Conceptual scheme of zeroth persistent homology determined about a randomly selected pair of pores (2-column fitting image)

The barycentric positions of all the pores, converted as diameters of their equivalent volume spheres, were obtained using Amira™ software (Thermo Fisher Scientific). The persistent pairs were simulated using the free software HomCloud developed by Obayashi et al. at Hiraoka Laboratory at Center for Advanced Intelligence Project in RIKEN [30], and pores smaller than 78 μm^3 were omitted to consider the effect of background noise in the X-ray laminography observation.

3. Results

Fig. 2 shows the stress-strain (S-S) curve obtained during the in-situ tensile test carried out concurrently with the X-ray laminography scanning. The scans were executed at plastic deformations of ε_p = 0, 0.025, 0.039, 0.060, 0.062, and 0.140 after each unloading, as

indicated by the arrows. The last scan required an interval exceeding 3700 ks owing to the allocation of the operating time of the synchrotron, whereas the first four scans required ~9 ks intervals. As in the S-S curve, notable increases were seen in the stress before the final scan. This may be attributable to the occurrence of a kind of stress aging owing to the migration of carbon atoms that are inevitably present to the dislocation site during a long interval.

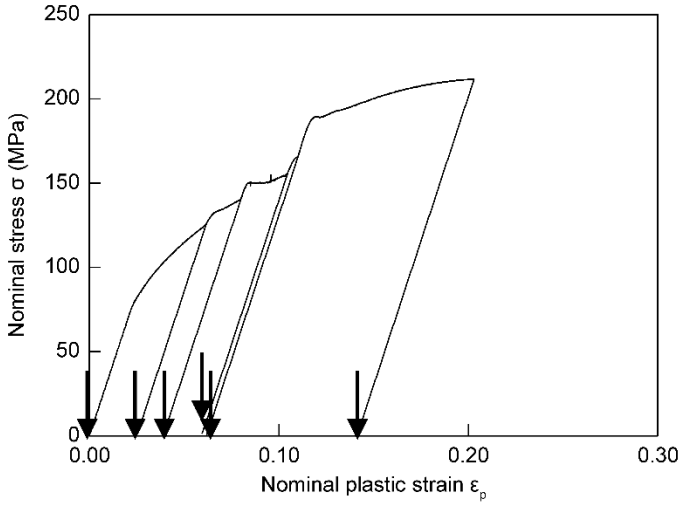

Fig. 2. Representative stress-strain (S-S) curve of the specimen from tensile tests carried out in the intervals between allowed X-ray CT scanning points. (single-column fitting image)

Fig. 3 shows a 3D pore image with 1 mm cubic scale of the inner pores in the unloaded specimen. Projection images from laminograpy were reconstructed into a cylindrical shape with 1000 μm diameter and 1000 μm thickness. In the 3D pore image shown in Fig. 3 and the following figures, red cavities indicate open pores that connect from the interior to the plane of the columnar observation area, and other colours indicate isolated closed pores. Because the pore distribution was too intricate to scrutinize the inside structure from the surface, 3D images with slices of z = 750–1000 μm were obtained, as shown in Fig. 4. The open pore network was spread throughout the specimen, and it expanded with increasing strain up to a width of ~20 μm around its branching area at ε_p = 0.140. By contrast, a notable change in the configuration of the closed pores in the interstitial spaces of

the open pore network could not be visually confirmed. Therefore, we focused on the configurational change of the open and closed pores, especially around the branching of the open pore, by using the zeroth PH.

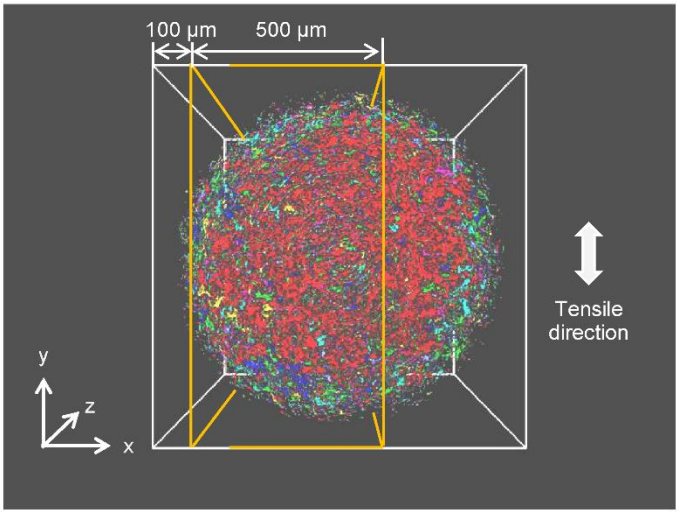

Fig. 3. 3D snapshot of pores in 1 mm cubic scale at $\varepsilon_p = 0$. Analysis by persistent homology was carried out for areas marked by orange lines with slices at x = 100–600 mm. (single-column fitting image)

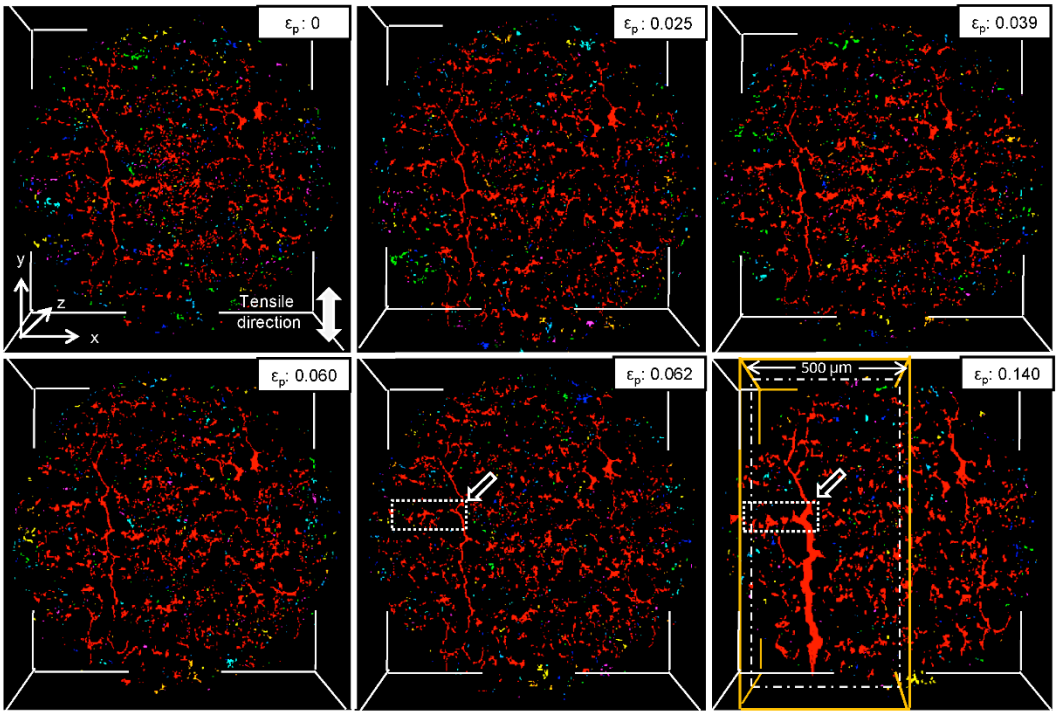

Fig. 4. 3D snapshots of pores in 1 mm cubic sliced at planes with 1/4 thickness from the

surface at z = 1000 μm at ε_p = 0–0.140. (2-column fitting image)

4. Discussion

4.1. Connections between open pore and closed pores estimated from PH

For the PH analysis, we used 3D images with slices of x = 100–600 μm, including the area where the open pore branched, as indicated by the orange line in Fig. 4 at ε_p = 0.140. PD0 was lined up for all pores (Fig. 5), and only the closed pores (Fig. 6) in the sliced area. The characteristic distributions are indicated by the surrounding dotted lines. The plots in areas B and C showed common distributions, whereas the plot in area A was confirmed only in Fig. 5. It follows that these configurations indicate the connections between the open pore and surrounding closed pores under each strain. In fact, plots of $\{d_i\}$ in area A were 50–280 μm from the initial to the final stage; this was comparable to the r_{i0} of the open pores (200–220 μm). Notably, $\{d_i\}$ in area A increased from ε_p = 0.060 to 0.062 and drastically decreased at ε_p = 0.140 just before fracturing. Such increases and decreases might correspond to secondary void generation adjacent to the swelling of the open pore and the disappearance of closed pores by the adsorption of the open pore, respectively, resulting in the growth of the crack.

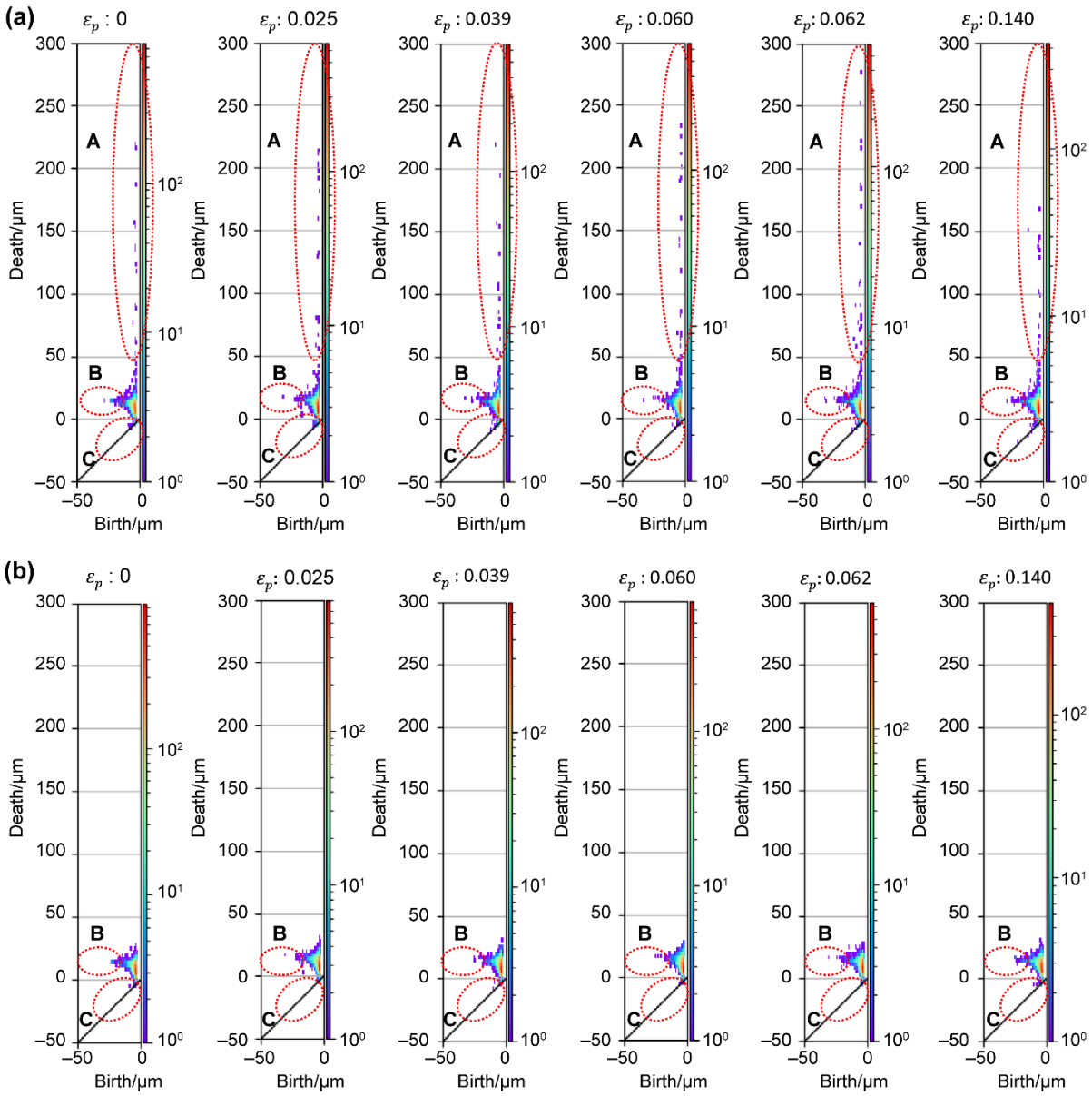

Fig. 5. (A) Zeroth persistent diagram, PD0, about pores including an open pore in the area sliced with x = 100–600 mm during the tensile test. (B) Zeroth persistent diagram, PD0, about pores WITHOUT an open pore in the area sliced with x = 100–600 mm during the tensile test. (2-column fitting image)

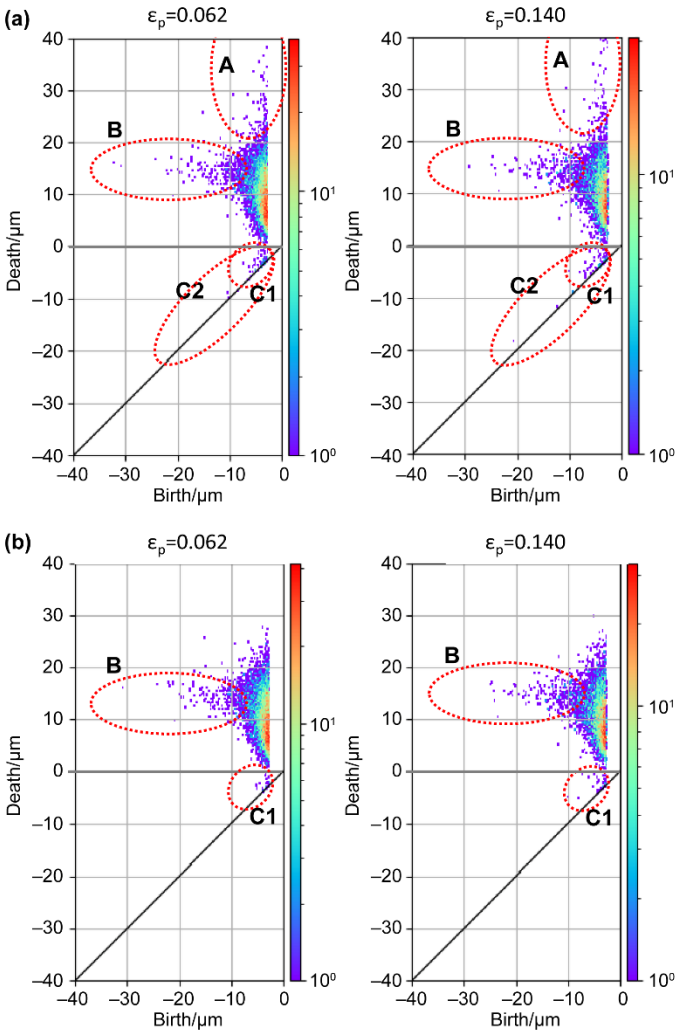

Fig. 6. Magnified images of PD0 about pores in the area sliced with x = 100–600 mm during the tensile test: (a) including an open pore and (b) without an open pore. (1.5-column fitting image)

4.2. Mutual connections between closed pores estimated from PH

To confirm the change in PD0 at around the final stage, a magnified view of PD0s at ε_p = 0.062 and 0.140 is shown in Fig. 6(a) for all pores including the open pore and in Fig. 6(b) without. As mentioned above, the distribution in areas B and C concerned the mutual connections between closed pore pairs. In area B, the increment in $|b_i|$ (= r_{i0}) at ε_p = 0.140 can correspond to the growth of closed pores owing to the elongation of the specimen along the tensile direction without significant changes in the mutual distance. In the third quadrant

of PD0, the plots in area C1 are seen in both Figs. 6(a) and 6(b), whereas those in area C2 are seen only in Fig. 6(a). The $|d_i|$ values in both areas, which correspond to the overwrapped volumes between pores in pairs, increased at ε_p = 0.140. This strongly suggested that the closed pores approached not only the open pore but also other closed pores, resulting in the formation of ductile cracks.

4.3. Pore connections estimated from 4D pore images

To confirm the change in pore configurations suggested by PD0, enlarged views of the 3D CT images around the area at ε_p = 0.062 and 0.140, where the open pore branched as indicated in Fig. 4, are shown in Fig. 7. The closed pores beside the red-coloured open pore in Fig. 7a are considered to correspond to the configurations in area A or C2 in Fig. 6a from the relation to the open pore and to those in area B from the relation to the adjacent closed pores, as mentioned above. Some of them, indicated by dotted circles, are adsorbed by the open pore and diminished, as shown in Fig. 7b. By contrast, elongated closed pores with a higher aspect ratio that surrounded the dotted circles in Figs. 7a and 7b were positioned close to each other; therefore, their equivalent volume spheres can overwrap, as estimated from area C1 in the PD0s shown in Figs. 6a and 6b. Fig. 8 shows the number of porosities of the open and closed as well as those of all pores. Fig. 9 shows the average aspect ratio of closed pores obtained from 4D images. Notably, pore volumes obtained from the 3D analysis were underestimated compared to the actual values because the voxels at the boundary area between the matrix and pore were considered to possess a matrix volume and not as pore volume, even if the voxel contained a part of the pore. The total porosity at ε_p = 0 was calculated as 7.2% from the 3D image in Fig. 3, with a voxel size of 0.5 μm, which is 4.5% lower than that (11.7%) obtained using the Archimedes' method. The total porosity, open porosity, and aspect ratio increased, while the closed porosity decreased with increasing

strain, thereby supporting the claim that the elongated closed pores approach and merge with other open/closed pores. These close-set configurations of pores were seen in the area from the branch point of the open pore to the surface along the direction perpendicular to the tensile stress. It can be predicted that these pores will be subjected to compressive stress during the local deformation stage and will eventually coalesce to form a ductile fracture crack characterized by a fracture surface with fine dimples.

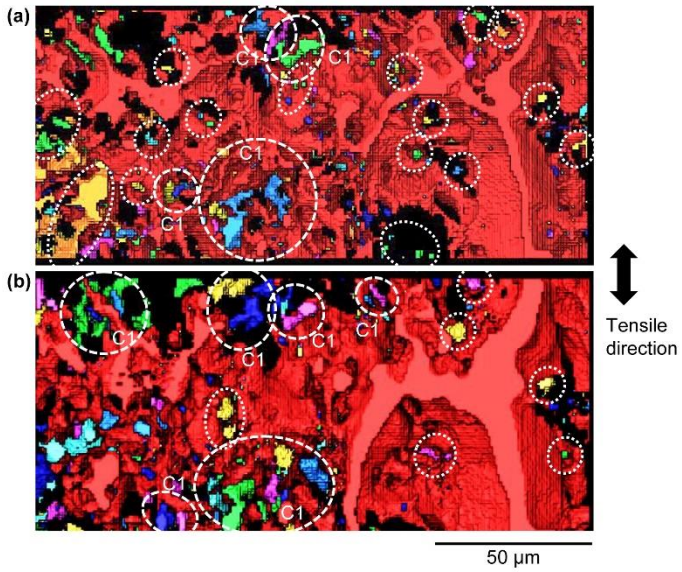

Fig. 7. Enlarged 3D images sliced at the planes with 1/4th thickness from the surface at z = 1000 μm at (a) ε_p = 0.062 and (b) ε_p = 0.140. C1 corresponds to PD0 in Fig. 6. (single-column fitting image)

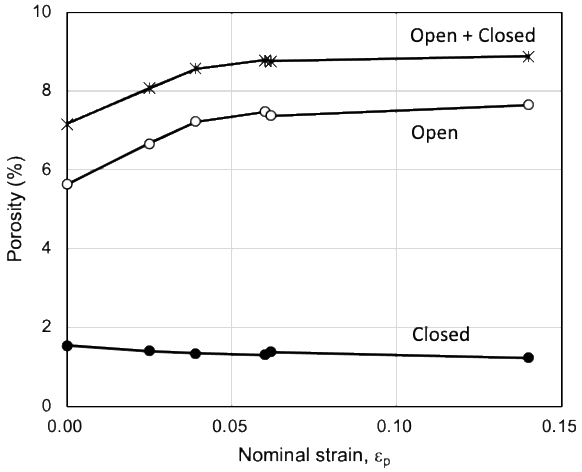

Fig. 8. Dependence of open/closed and total porosities in the sintered iron on nominal strain

during tensile test. (single-column fitting image)

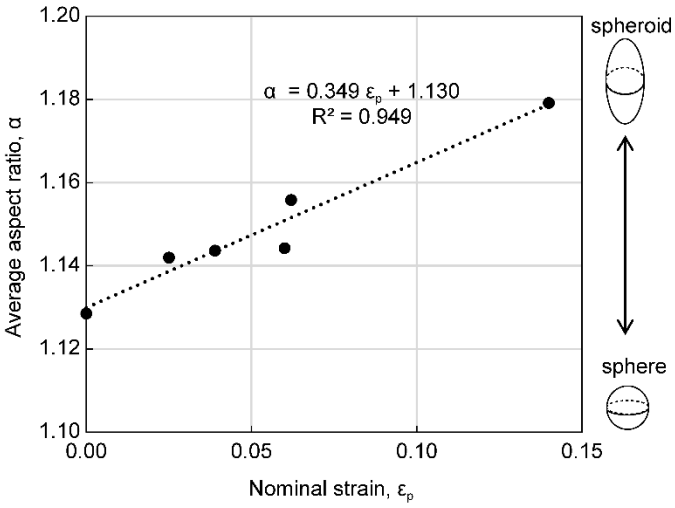

Fig. 9. Dependence of average pore ratio in sintered iron on nominal strain during tensile test. (single-column fitting image)

5. Conclusion

4D images of pores in a sintered pure iron specimen with 11% porosity were obtained thorough synchrotron X-ray laminography during tensile tests. The pore configurations were quantified, and their changes under increased strains were tracked quantitatively using an algebraic topology, PH. This study adopted the zeroth PH, for which the radius of the equivalent volume sphere of each pore and the distance to another pore between pores can be estimated from the birth and death values (b_i, d_i) , respectively. The connection process of pores or microvoids was clarified as follows:

(1) During a tensile test, 3D images of the inside of the specimen can be obtained at nominal strains of ε_p = 0–0.140, and the process whereby open pores swelled up and branched perpendicular to the tensile stress in the centre of the specimen was confirmed to occur.

(2) The pore configurations can be quantified as a set of 2D numbers $\{(b_i, d_i)\}$, and the changes due to increasing strain were tracked.

(3) By comparing PD0, where $\{(b_i, d_i)\}$ is plotted on the (x, y)-plane, for pores including/without an open pore, the characteristic changes of pore configurations consisting of open pores can be confirmed at the final stage (ε_p = 0.140).

(4) Such characteristic changes indicated that (i) the pair configurations between the open pore and closed pores for d > 50 μm decreased owing to the adsorption of the closed pores by the open pore, and (ii) the pair configurations of the elongated pores and the open pore, whose equivalent volume spheres are overwrapped, increased.

(5) The changes in 3D images from ε_p = 0.620 to 0.140 were confirmed to reasonably correspond to the above topological information.

In conclusion, we could clarify the role of open pores independently of that of closed pores in the process of ductile crack initiation by using the zeroth PH. This facilitates the interpretation of the pore connection process that is essential for ductile crack generation. In the future, we will investigate the ductile fracture mechanism in high-density sintered metals in which open pores are blocked and in hot isostatically pressed PM materials without any pores to conclude whether the fracture mechanism of PM metals becomes congruent with that of wrought metals.

Acknowledgements

Synchrotron radiation experiments were performed at the BL20XU beamline of SPring-8 with the approval of Japan Synchrotron Radiation Research Institute (JASRI) (Proposal No. 2018B1263). This work was also partially supported by I^2CNER at Kyusyu University. We thank JFE Steel Co. for preparing the sintered specimens. We are grateful to Professors Masato Niibe, Hiroki Adachi, and Hiroyuki Toda for their assistance with our work at SPring-8. We are also grateful to Professor Tomoyuki Shirai for the helpful discussions on PH analysis. We thank Dr. Ippei Obayashi and Professor Yasuaki Hiraoka at the Center for

Advanced Intelligence Project (AIP) in RIKEN for providing the free software “HomCloud” and their appropriate advice. We would like to thank Editage (www.editage.com) for English language editing.

Funding: This work was supported in joint research with JFE Steel Corporation.

Declarations of interest: None.

Data Availability Statement:

The raw/processed data required to reproduce these findings cannot be shared at this time due to legal or ethical reasons.

References

[1] P.K. Jones, K. Buckley-Golder, H. David, R. Lawcock, D. Sarafinchan, R. Shivanath, L. Yao, Fatigue properties of advanced high density powder metal alloy steels for high performance powertrain applications, Proc. 1998 PM World Cong., Granada, Spain, EPMA, Shrewsbury, UK, 3 (1998) 150-166.

[2] H.G. Rutz, F.G. Hanejko, High density processing of high performance ferrous materials, Adv. Powder Metall. Part. Mater. 5 (1994) 117-140.

[3] T. Hayasaka, Development of high-strength PM machine parts, J. Jap. Soc. Powder Metal. 33 (1986) 1-10.

[4] H. Danninger, D. Spoljaric, G. Jangg, B. Weiss, R. Stickler, Characterization of Pressed and Sintered Ferrous Materials by Quantitative Fractography, Pract. Metallogr. 31 (1994)56-69.

[5] H. Danninger, D. Spoljaric, B. Weiss, Microstructural features limiting the performance of P/M steels, Int. J. Powder Metall. 33 (1997) 43-53.

[6] H. Danninger, B. Weiss, The influence of defects on high cycle fatigue of metallic materials, J. Mater. Process. Technol. 143-144(2003) 179-184.

[7] M. Slesar, E. Dudrová, E. Rudnayova, Plain porosity as a microstructural characteristic of sintered materials, Powder Metall. Int. 24 (1992) 232-236.

[8] J.M. Torralba, L. Esteban, E. Bernardo, M. Campos, Understanding contribution of microstructure to fracture behavior of sintered steels, Powder Metall. 57 (2014) 357.

[9] E. Dudrová, M. Kabatová, Fractography of sintered iron and steels, Powder Metall. Prog., 8 (2008) 59-75.

[10] E. Dudrová, M. Kabátová, A review of failure of sintered steels: fractography of static and dynamic crack nucleation, coalescence, growth and propagation, Powder Metall. 59 (2016) 148-167.

[11] P.F. Thomason, A theory of ductile fracture by internal necking of cavities, J. Inst. Met. 96 (1968) 360-365.

[12] F.A. McClintock, A criteria for ductile fracture by the growth of holes, J. Appl. Mech. 35(1968) 363-371.

[13] T.B. Cox, J.R. Low, An investigation of the plastic fracture of AISI 4340 and 18 nickel--200 grade maraging steels, Metall. Trans. 5 (1974) 1457-1470.

[14] H. Toda, I. Sinclair, J.-Y. Buffiere, E. Maire, T. Connolley, M. Joyce, K.H. Khor, P. Gregson, Assessment of the fatigue crack closure phenomenon in damage-tolerant aluminum alloy by in-situ high-resolution synchrotron X-ray microtomography, Phil. Mag. A. 83 (2003) 2429-2448.

[15] H. Toda, I. Sinclair, J.-Y. Buffiere, E. Maire, K.H. Khor, P. Gregson, T. Kobayashi, A 3D measurement procedure for internal local crack driving forces via synchrotron X-ray microtomography, Acta Mater. 52 (2004) 1305-1317.

[16] L. Qian, H. Toda, K. Uesugi, T. Kobayashi, T. Ohgaki, M. Kobayashi, Application of synchrotron x-ray microtomography to investigate ductile fracture in Al alloys, Appl. Phys. Lett. 87 (2005) 241907-1-241907-1-3.

[17] T. Ohgaki, H. Toda, M. Kobayashi, K. Uesugi, M. Niinomi, T. Akahori, T. Kobayashi, K. Makii, Y. Aruga, In situ observations of compressive behaviour of aluminium foams by local tomography using high-resolution X-rays, Philos. Mag. A 86 (2006) 4417-4438.

[18] H. Toda, K. Uesugi, A. Takeuchi, K. Minami, M. Kobayashi, T. Kobayashi, Three-dimensional observation of nanoscopic precipitates in an aluminum alloy by microtomography with Fresnel zone plate optics, Appl. Phys. Lett. 89 (2006) 143112-1-143112-3.

[19] M. Kobayashi, H. Toda, K. Uesugi, T. Ohgaki, Kobayashi, Y. Takayama, B.-G. Ahn, Preferential penetration path of gallium into grain boundary in practical aluminium alloy,

Phil. Mag. A 86 (2006) 4351-4366.

[20] O. Furukimi, Y. Takeda, M. Yamamoto, M. Aramaki, S. Munetoh, A. Takeuchi, H. Ide, M. Nakasaki, Voids nucleation and growth examination during tensile deformation for IF steel by synchrotron X-ray laminography and EBSD, Tetsu-to-Hagane, 103 (2017) 475-482.

[21] N. Chawla, S. J. Polasik, K. S. Narasimhan, T.Murphy, M. Koopman, K.K. Chawla, Fatigue behavior of binder-treated P/M steels, Int. J. Powder Metall., 37(2001)49-57.

[22] S. J. Polasik, J.J. Williams, N. Chawla, Fatigue crack initiation and propagation of binder-treated powder metallurgy steels, Metall. Mater. Trans. A, 33 (2002) 73-81.

[23] N. Chawla, X. Deng, Microstructure and Mechanical Behavior of Porous Sintered Steels, Mater. Sci. Eng. A, 390 (2005) 98-112.

[24] N. Chawla, J.J. Williams, X. Deng, C. McClimon, L. Hunter, S.H. Lau, Three-dimensional characterization and modeling of porosity in PM steels, Int. J. Powder Metall. 45 (2009) 19-27.

[25] Y. Ozaki, Y. Mugita, M. Aramaki, O. Furukimi, S. Oue, F.Jiang, T.Tsuji, A. Takeuchi, M. Uesugi, K. Ashizuk, Four-dimensional observation of ductile fracture in sintered iron using synchrotron X-ray laminography, Powder Metall. 62 (2019) 146-154.

[26] S. Gondrom, J. Zhou, M. Maisl, H. Reiter, M. Kröning, W. Arnold, X-ray computed laminography: an approach of computed tomography for applications with limited access, Nucl. Eng. Des. 190 (1999) 141-147.

[27] L. Helfen, T. Baumbach, P. Mikulík, D. Kiel, P. Pernot, P. Cloetens, J. Baruchel, High-resolution three-dimensional imaging of flat objects by synchrotron-radiation computed laminography, Appl. Phys. Lett. 86 (2005) 071915-1-071915-3.

[28] M. Hoshino, K. Uesugi, A. Takeuchi, Y. Suzuki, N. Yagi, Development of an X-ray Micro-Laminography System at SPring-8, AIP Conf. Proc. 1365 (2011) 250-253.

[29] I. Obayashi, Volume-Optimal Cycle: Tightest Representative Cycle of a Generator in

Persistent Homology, SIAM J. Appl. Algebra Geometry, 2 (2018) 508-534.

[30] HomCloud. https://homcloud.dev/index.html.

Elucidation of pore connection mechanism during ductile fracture of sintered pure iron by applying persistent homology to 4D images of pores: Role of open pore

Isshin Ando[a], Yasutaka Mugita[a], Kyosuke Hirayama[b], Shinji Munetoh[a], Masatoshi Aramaki[a], Fei Jiang[c], Takeshi Tsuji[d], Akihisa Takeuchi[e], Masayuki Uesugi[e] and Yukiko Ozaki[a]*

[a] Department of Materials Science and Engineering, Kyushu University, 744, Motooka, Nishi-ku, Fukuoka 819-0395, Japan

[b] Department of Materials Science and Engineering, Kyoto University, Yoshida-honmachi, Sakyo-ku, Kyoto 606-8501, Japan

[c] Department of Mechanical Engineering, Yamaguchi University, 12-16-1, Tokiwadai, Ube, Yamaguchi 755-8611, Japan

[d] Department of Earth Resources Engineering, Kyushu University, 744, Motooka, Nishi-ku, Fukuoka 819-0395, Japan

[e] Japan Synchrotron Radiation Research Institute (JASRI), 1-1-1, Kouto, Sayo-cho, Sayo-gun, Hyogo 679-5198, Japan

*Corresponding author: Yukiko Ozaki

Department of Materials Science and Engineering, Kyushu University

744, Motooka, Nishi-ku, Fukuoka 819-0395, Japan

Phone: +81-92-802-2941

Fax: +81-92-802-2990

E-mail: ozaki@zaiko.kyushu-u.ac.jp

Abstract

4D pore configurations including an open pore were visualized by synchrotron X-ray laminography during the ductile fracturing process and then interpreted quantitatively using persistent homology (PH), a topological measure. In particular, this study used the zeroth PH, where the radius of an equivalent volume sphere for each pore and the distances to the other pores can be estimated for pairs of pores. The pore configurations were quantified as a set of birth and death values $\{(b_i, d_i)\}$ and changes due to increasing strain were tracked. As a result, the zeroth PH revealed the following information at the final stage before fracturing. First, the pair configurations between the open pore and closed pores decreased owing to the adsorption of closed pores by the open pore. Second, the configuration between the elongated closed pore and the open pore, where equivalent volume spheres are overwrapped, increased. These configurational changes in pores predict the pore connection between the open pore and surrounding closed pores that eventually generates a ductile crack perpendicular to the tensile stress. This study demonstrated the effective interpretation of the pore connection process that is essential to ductile crack generation.

Keywords: ductile fracture, sintered iron, open pore, closed pore, persistent homology

1. Introduction

Powder metallurgical (PM) automobile parts must be downsized to achieve zero emissions. Toward this end, high-density compaction processes [1,2] such as double press double sintering (DPDS) and warm compaction (WC) are currently available. However, such high-density PM materials still contain pores, and therefore, their mechanical properties are not comparable to those of wrought steel [3]. The effects of such pores on crack initiation must be clarified to improve the reliability of PM materials for use as structural members. In recent years, several studies have investigated the fracture mechanisms and crack morphologies of fractured PM steels [4-10]. Torralba et al. conducted in-situ observations under loads using a scanning electron microscope (SEM) with a digital image correlation technique and found that initial cracks were generated from sharp pores with a high aspect ratio or in the area where Kirkendall pores formed in heterogeneous diffusion alloyed Fe–Ni–Cu–Mo–C steel propagated immediately to neighbouring pores in the sintered metallic steels [8]. Dudrová and Kabátová systematically reviewed the fractography of sintered Fe-Cu-C, Fe- 1.8% Cr and 4% Ni diffusion-bonded alloyed steel [9,10]. Nonetheless, proposing a suitable theoretical model for PM materials in a manner similar to those proposed for bulk materials [11-13] remains difficult because the sintered bodies contain hundreds of thousands of micropores or microcracks.

High-intensity X-ray computation tomography (CT) has used for observing microvoid initiation under a tensile load in wrought metals. Toda et al. conducted X-ray microtomography at Spring-8 to visualize the crack extending process under tensile loads between coarse micropores as snapshots for Al-based alloys containing Zn or Mg [14-19]. Furukimi et al. used a 4D technique with tensile tests and found that micropores around grain boundaries coalesced into cracks owing to the strain concentrations in industrial pure-iron sheets [20]. Chawla et al. first applied a 3D-CT technique to unloaded sintered metals and

then visualized the local stress concentration between pores using finite element models under tensile loads based on the pore configuration obtained from the 3D-CT images [21-24]. However, secondary initiated microvoids have not yet been tracked.

The authors have previously used synchrotron X-ray laminography to clarify the change process of pore configurations in sintered pure iron during a tensile test and demonstrated the applicability of persistent homology (PH), a type of topological analysis, to extract the configuration for < 3000 closed pores during the crack initiation stage within the confined area of a roughly 100-μm-thick slice without open pores [25]. In the present study, we investigated the role of open pores independently of that of closed pores by focusing on the mathematical connections between pores using PH. For this purpose, we considered more than 10^5 pores.

2. Experimental

2.1. Materials and specimen preparation for tensile test

The tensile test was conducted using a sintered pure iron powder specimen (JFE Steel Co., JIP301A) that was prepared as reported previously [25]. The specimen porosity was 11.7%, and it included open and closed pores as determined using Archimedes' water immersion technique. Further, it had dimensions of 2 mm (width), 1 mm (thickness), and 3 mm (length) in the centre area, and it was machined using a wire electric discharge machine.

2.2. In-situ 4D observation during tensile test by synchrotron X-ray laminography

High-resolution X-ray laminography experiments were performed at the BL20XU X-ray imaging beamline at SPring-8, where the maximum spatial resolution for volume reconstruction was around 1 μm and the minimum voxel size was as low as 0.3 μm [26-28]. The photon energy of the monochromatic X-ray beam generated by the liquid-nitrogen-

cooled Si (111) double-crystal monochromator was 37.7 keV. The specimen was placed on a rotatable stage, and the rotation axis was inclined at 45° to the X-ray beam. The detector was placed 18.0 mm from the centre of rotation on the specimen surface. A radiograph with a diameter of 1000 μm was taken about the centre area of the specimen with an exposure time of 300 ms at every 0.1° during a rotation. The captured images were reconstructed with isotropic voxels having a size of 0.5 μm from a series of radiographs by the filtered back projection algorithm and visualized as 3D images using the image-analysis software Avizo 9.1.1 (FEI Co.).

The laminography scans were performed before the tensile test at five distinct plastic deformations at every moment when the tensile test was interrupted and the load, applied at a constant strain rate of 10^{-3} s^{-1}, was discharged.

2.3. Analysis of connection between pores by PH

PH is a topological measure that quantifies point cloud configurations as 2D values [29]. In this method, the radius r of a sphere that is virtually placed at each point is increased from 0. As r increases, holes formed by the contact or overlap of spheres at specific points are created or disappear. Two radii—birth value b at the time when a hole surrounded by the spheres is generated and death value d when the hole disappears—are used. The persistent pair (b, d) corresponds to the point cloud configuration. As a result, the finite set of persistent pairs for n point cloud configurations, $\sum_{i=1}^{n}\{(b_i, d_i)\}$, can be plotted on the (x, y)-plane to produce the persistence diagram (PD). In 3D space, PD is defined from the zeroth to the second PD, that is, PD0, PD1 and PD2; these are respectively the configurations for two-point connections, more than three-points connections forming polygons, and more than four-points forming polyhedrons. A void-connection model has been proposed for the ductile fracture of metallic materials. Therefore, in this study, the remaining pores and microvoids

were considered point clouds, and the zeroth PD was applied to quantitatively analyse their connection process.

The zeroth PH for the pore group in sintered materials is as follows. Figs. 1a and 1b (left) illustrate the process of obtaining PD0 about a pair of a randomly selected i-th sphere pore and its adjacent pore. In the initial state, a sphere with an equivalent volume is placed at the barycentre of each pore. Then, these spheres are expanded or shrunk depending on whether they overlap (Case I or II). b_i is defined as the reverse-signed initial radius r_{i0} of the i-th sphere on the left. The pair (b_i, d_i) of two spheres is defined as follows:

$$b_i \equiv -r_{i0}\ (<0), \quad (1)$$

$$d_i \equiv sgn\ (\Delta) \times \sqrt{|\Delta|}, \quad (2)$$

$$\Delta \equiv r_{if}^2 - r_{i0}^2. \quad (3)$$

In Eq. 3, r_{if} is the radius of the i-th sphere at contact. $sgn\ (\Delta)$ is negative in Case II where two spheres with equivalent volumes overlap as for neighboring pores with high aspect ratio. As shown in Figs. 1a and 1b for the final case at contact, a death value d_i, which indicates the length of a generatrix line formed by the initial sphere and the contacting point at the final stage, corresponds to the distance between the sphere of interest and the adjacent sphere in both cases. Because the pair cloud $\{(b_i, d_i)\}$ in Cases I and II is respectively in the second and third quadrants, these cases can be easily distinguished on the (x, y)-plane.

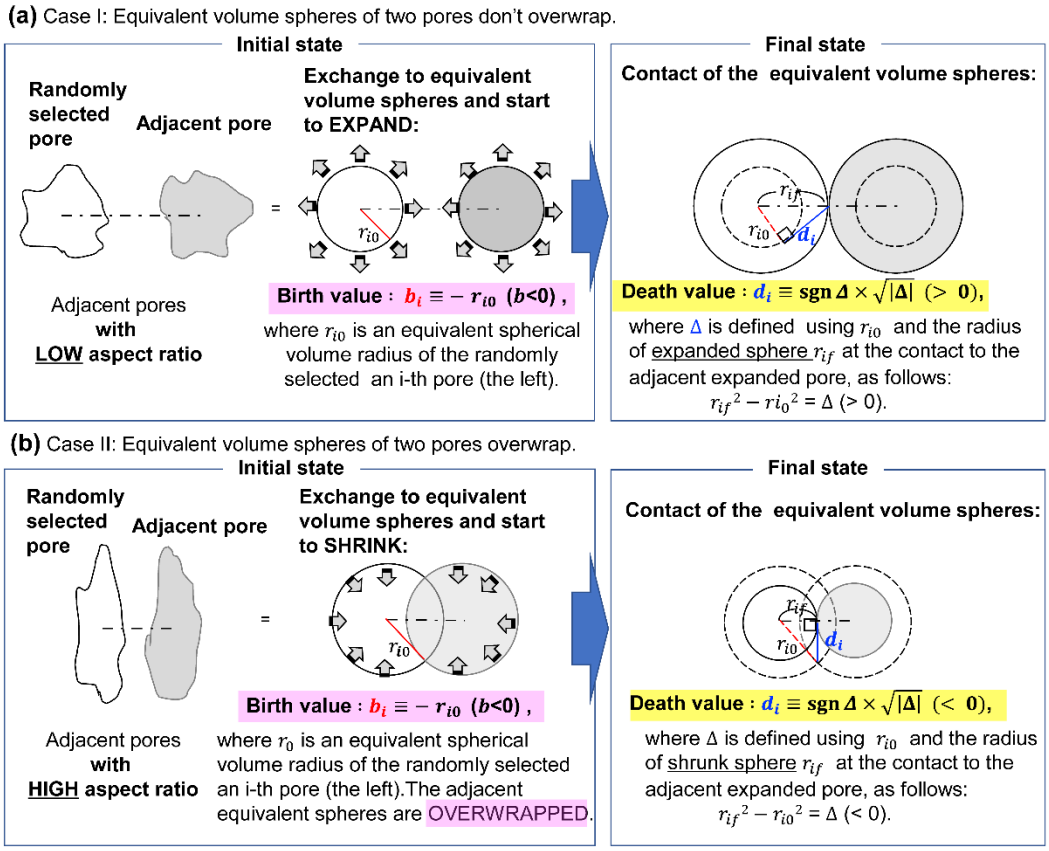

Fig. 1. Conceptual scheme of zeroth persistent homology determined about a randomly selected pair of pores (2-column fitting image)

The barycentric positions of all the pores, converted as diameters of their equivalent volume spheres, were obtained using Amira™ software (Thermo Fisher Scientific). The persistent pairs were simulated using the free software HomCloud developed by Obayashi et al. at Hiraoka Laboratory at Center for Advanced Intelligence Project in RIKEN [30], and pores smaller than 78 μm^3 were omitted to consider the effect of background noise in the X-ray laminography observation.

3. Results

Fig. 2 shows the stress-strain (S-S) curve obtained during the in-situ tensile test carried out concurrently with the X-ray laminography scanning. The scans were executed at plastic deformations of ε_p = 0, 0.025, 0.039, 0.060, 0.062, and 0.140 after each unloading, as

indicated by the arrows. The last scan required an interval exceeding 3700 ks owing to the allocation of the operating time of the synchrotron, whereas the first four scans required ~9 ks intervals. As in the S-S curve, notable increases were seen in the stress before the final scan. This may be attributable to the occurrence of a kind of stress aging owing to the migration of carbon atoms that are inevitably present to the dislocation site during a long interval.

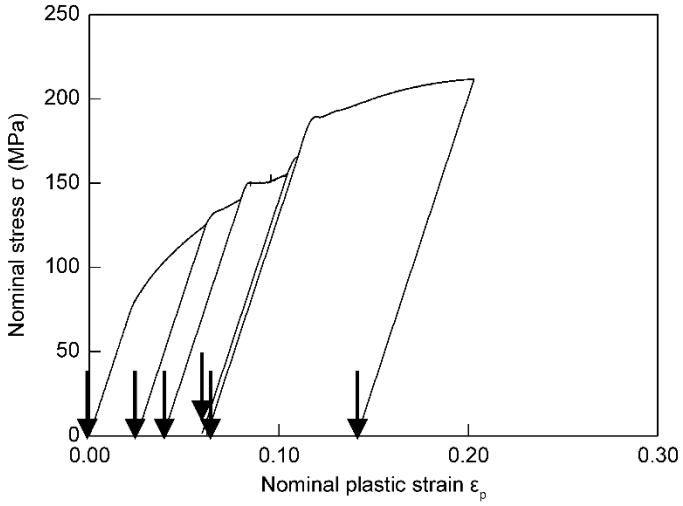

Fig. 2. Representative stress-strain (S-S) curve of the specimen from tensile tests carried out in the intervals between allowed X-ray CT scanning points. (single-column fitting image)

Fig. 3 shows a 3D pore image with 1 mm cubic scale of the inner pores in the unloaded specimen. Projection images from laminograpy were reconstructed into a cylindrical shape with 1000 μm diameter and 1000 μm thickness. In the 3D pore image shown in Fig. 3 and the following figures, red cavities indicate open pores that connect from the interior to the plane of the columnar observation area, and other colours indicate isolated closed pores. Because the pore distribution was too intricate to scrutinize the inside structure from the surface, 3D images with slices of z = 750–1000 μm were obtained, as shown in Fig. 4. The open pore network was spread throughout the specimen, and it expanded with increasing strain up to a width of ~20 μm around its branching area at ε_p = 0.140. By contrast, a notable change in the configuration of the closed pores in the interstitial spaces of

the open pore network could not be visually confirmed. Therefore, we focused on the configurational change of the open and closed pores, especially around the branching of the open pore, by using the zeroth PH.

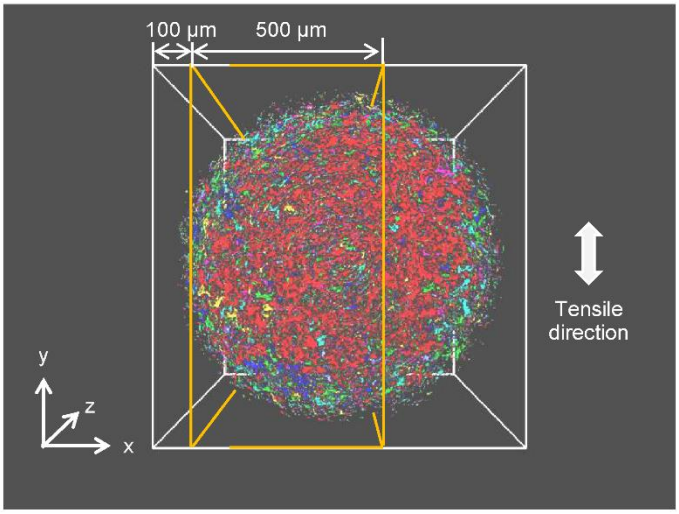

Fig. 3. 3D snapshot of pores in 1 mm cubic scale at $\varepsilon_p = 0$. Analysis by persistent homology was carried out for areas marked by orange lines with slices at x = 100–600 mm. (single-column fitting image)

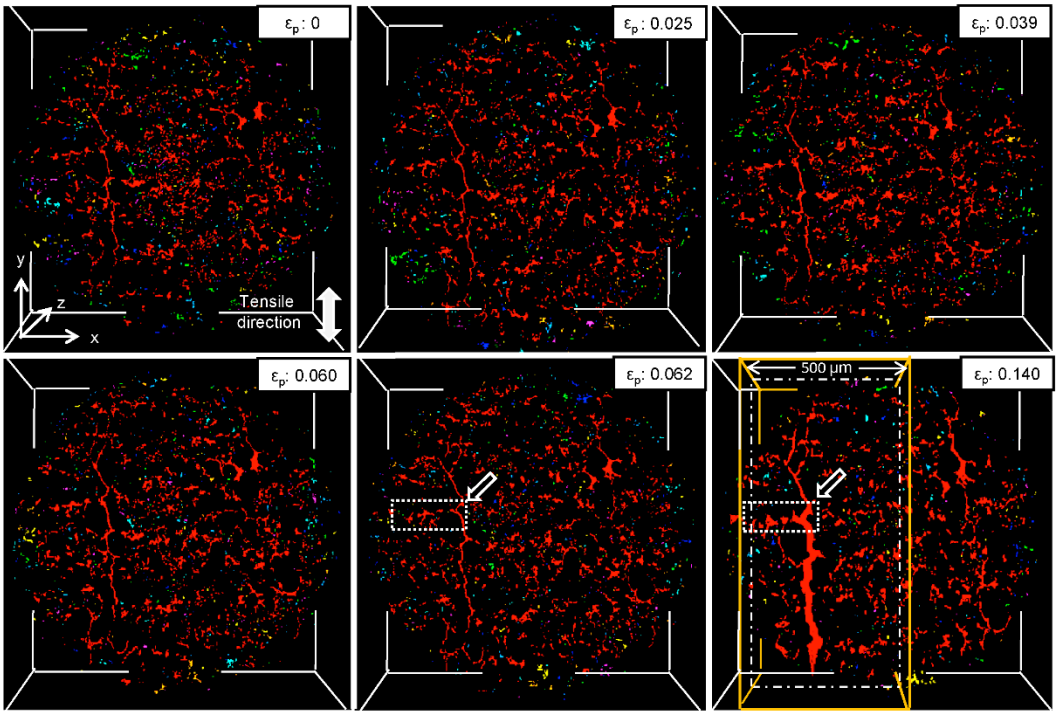

Fig. 4. 3D snapshots of pores in 1 mm cubic sliced at planes with 1/4 thickness from the

surface at z = 1000 μm at ε_p = 0–0.140. (2-column fitting image)

4. Discussion

4.1. Connections between open pore and closed pores estimated from PH

For the PH analysis, we used 3D images with slices of x = 100–600 μm, including the area where the open pore branched, as indicated by the orange line in Fig. 4 at ε_p = 0.140. PD0 was lined up for all pores (Fig. 5), and only the closed pores (Fig. 6) in the sliced area. The characteristic distributions are indicated by the surrounding dotted lines. The plots in areas B and C showed common distributions, whereas the plot in area A was confirmed only in Fig. 5. It follows that these configurations indicate the connections between the open pore and surrounding closed pores under each strain. In fact, plots of $\{d_i\}$ in area A were 50–280 μm from the initial to the final stage; this was comparable to the r_{i0} of the open pores (200–220 μm). Notably, $\{d_i\}$ in area A increased from ε_p = 0.060 to 0.062 and drastically decreased at ε_p = 0.140 just before fracturing. Such increases and decreases might correspond to secondary void generation adjacent to the swelling of the open pore and the disappearance of closed pores by the adsorption of the open pore, respectively, resulting in the growth of the crack.

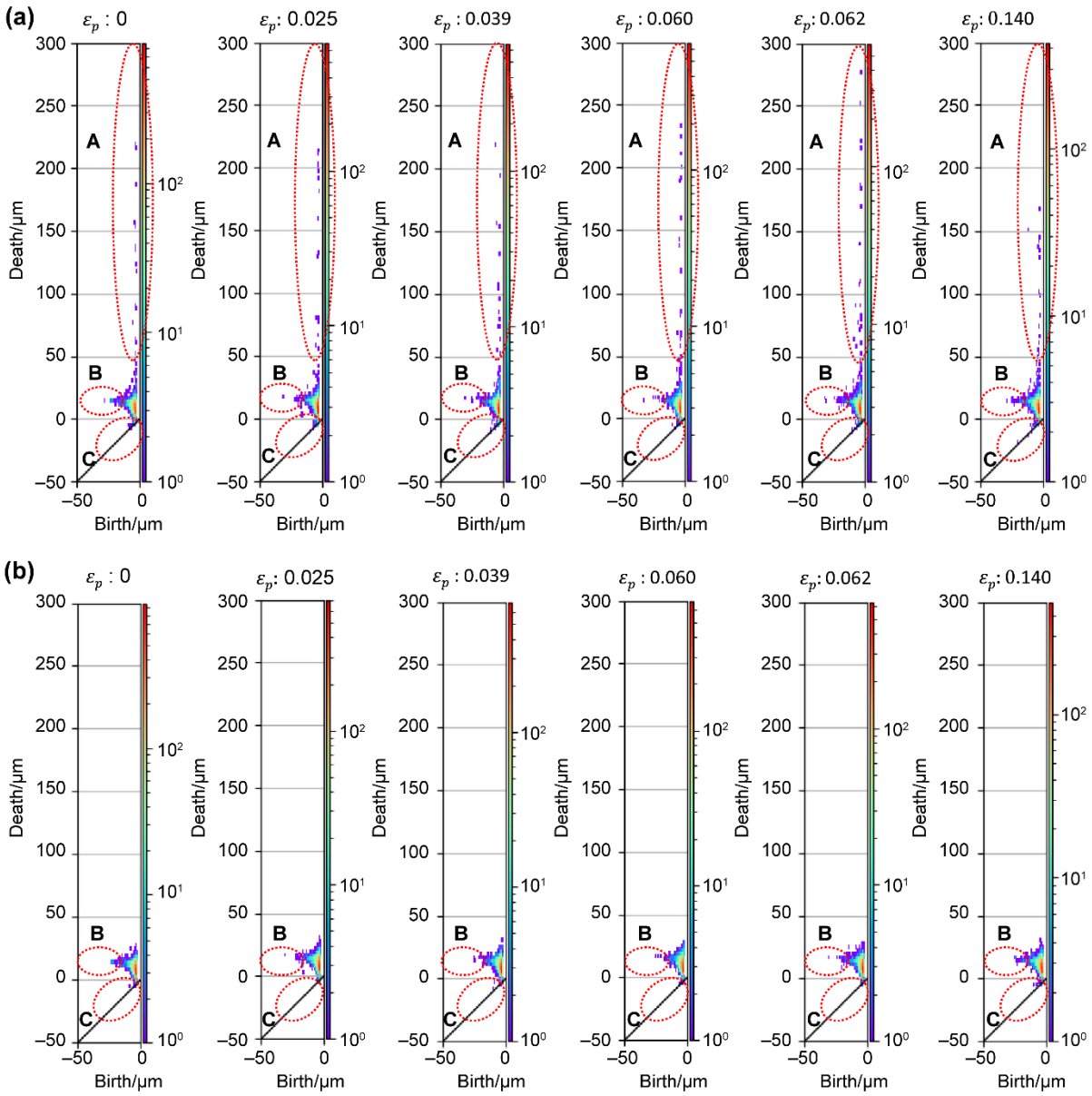

Fig. 5. (A) Zeroth persistent diagram, PD0, about pores including an open pore in the area sliced with x = 100–600 mm during the tensile test. (B) Zeroth persistent diagram, PD0, about pores WITHOUT an open pore in the area sliced with x = 100–600 mm during the tensile test. (2-column fitting image)

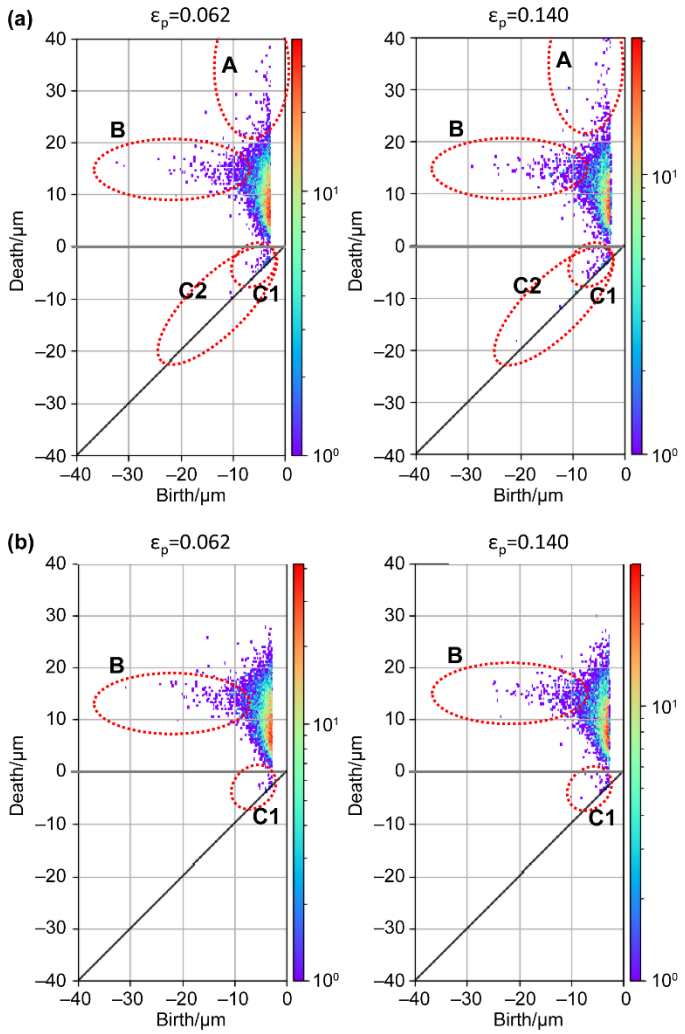

Fig. 6. Magnified images of PD0 about pores in the area sliced with x = 100–600 mm during the tensile test: (a) including an open pore and (b) without an open pore. (1.5-column fitting image)

4.2. Mutual connections between closed pores estimated from PH

To confirm the change in PD0 at around the final stage, a magnified view of PD0s at ε_p = 0.062 and 0.140 is shown in Fig. 6(a) for all pores including the open pore and in Fig. 6(b) without. As mentioned above, the distribution in areas B and C concerned the mutual connections between closed pore pairs. In area B, the increment in $|b_i|$ (= r_{i0}) at ε_p = 0.140 can correspond to the growth of closed pores owing to the elongation of the specimen along the tensile direction without significant changes in the mutual distance. In the third quadrant

of PD0, the plots in area C1 are seen in both Figs. 6(a) and 6(b), whereas those in area C2 are seen only in Fig. 6(a). The $|d_i|$ values in both areas, which correspond to the overwrapped volumes between pores in pairs, increased at $\varepsilon_p = 0.140$. This strongly suggested that the closed pores approached not only the open pore but also other closed pores, resulting in the formation of ductile cracks.

4.3. Pore connections estimated from 4D pore images

To confirm the change in pore configurations suggested by PD0, enlarged views of the 3D CT images around the area at $\varepsilon_p = 0.062$ and 0.140, where the open pore branched as indicated in Fig. 4, are shown in Fig. 7. The closed pores beside the red-coloured open pore in Fig. 7a are considered to correspond to the configurations in area A or C2 in Fig. 6a from the relation to the open pore and to those in area B from the relation to the adjacent closed pores, as mentioned above. Some of them, indicated by dotted circles, are adsorbed by the open pore and diminished, as shown in Fig. 7b. By contrast, elongated closed pores with a higher aspect ratio that surrounded the dotted circles in Figs. 7a and 7b were positioned close to each other; therefore, their equivalent volume spheres can overwrap, as estimated from area C1 in the PD0s shown in Figs. 6a and 6b. Fig. 8 shows the number of porosities of the open and closed as well as those of all pores. Fig. 9 shows the average aspect ratio of closed pores obtained from 4D images. Notably, pore volumes obtained from the 3D analysis were underestimated compared to the actual values because the voxels at the boundary area between the matrix and pore were considered to possess a matrix volume and not as pore volume, even if the voxel contained a part of the pore. The total porosity at $\varepsilon_p = 0$ was calculated as 7.2% from the 3D image in Fig. 3, with a voxel size of 0.5 μm, which is 4.5% lower than that (11.7%) obtained using the Archimedes' method. The total porosity, open porosity, and aspect ratio increased, while the closed porosity decreased with increasing

strain, thereby supporting the claim that the elongated closed pores approach and merge with other open/closed pores. These close-set configurations of pores were seen in the area from the branch point of the open pore to the surface along the direction perpendicular to the tensile stress. It can be predicted that these pores will be subjected to compressive stress during the local deformation stage and will eventually coalesce to form a ductile fracture crack characterized by a fracture surface with fine dimples.

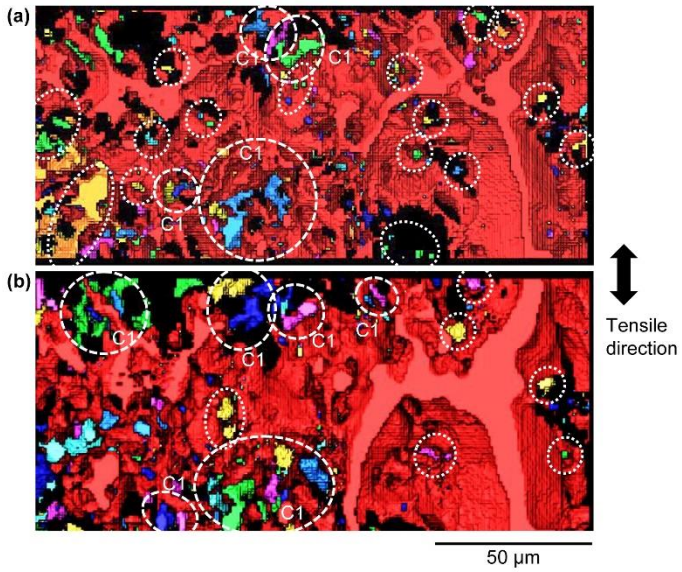

Fig. 7. Enlarged 3D images sliced at the planes with 1/4th thickness from the surface at z = 1000 μm at (a) ε_p = 0.062 and (b) ε_p = 0.140. C1 corresponds to PD0 in Fig. 6. (single-column fitting image)

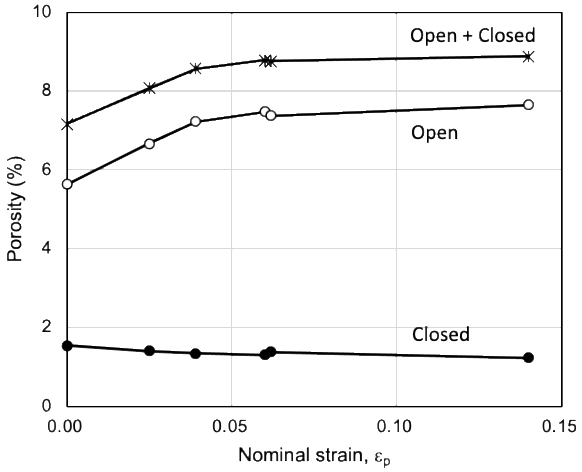

Fig. 8. Dependence of open/closed and total porosities in the sintered iron on nominal strain

during tensile test. (single-column fitting image)

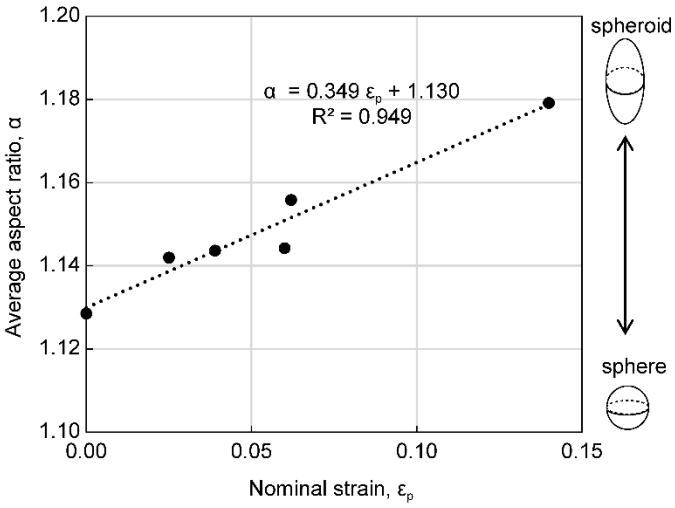

Fig. 9. Dependence of average pore ratio in sintered iron on nominal strain during tensile test. (single-column fitting image)

5. Conclusion

4D images of pores in a sintered pure iron specimen with 11% porosity were obtained thorough synchrotron X-ray laminography during tensile tests. The pore configurations were quantified, and their changes under increased strains were tracked quantitatively using an algebraic topology, PH. This study adopted the zeroth PH, for which the radius of the equivalent volume sphere of each pore and the distance to another pore between pores can be estimated from the birth and death values (b_i, d_i) , respectively. The connection process of pores or microvoids was clarified as follows:

(1) During a tensile test, 3D images of the inside of the specimen can be obtained at nominal strains of ε_p = 0–0.140, and the process whereby open pores swelled up and branched perpendicular to the tensile stress in the centre of the specimen was confirmed to occur.

(2) The pore configurations can be quantified as a set of 2D numbers $\{(b_i, d_i)\}$, and the changes due to increasing strain were tracked.

(3) By comparing PD0, where $\{(b_i, d_i)\}$ is plotted on the (x, y)-plane, for pores including/without an open pore, the characteristic changes of pore configurations consisting of open pores can be confirmed at the final stage (ε_p = 0.140).

(4) Such characteristic changes indicated that (i) the pair configurations between the open pore and closed pores for d > 50 μm decreased owing to the adsorption of the closed pores by the open pore, and (ii) the pair configurations of the elongated pores and the open pore, whose equivalent volume spheres are overwrapped, increased.

(5) The changes in 3D images from ε_p = 0.620 to 0.140 were confirmed to reasonably correspond to the above topological information.

In conclusion, we could clarify the role of open pores independently of that of closed pores in the process of ductile crack initiation by using the zeroth PH. This facilitates the interpretation of the pore connection process that is essential for ductile crack generation. In the future, we will investigate the ductile fracture mechanism in high-density sintered metals in which open pores are blocked and in hot isostatically pressed PM materials without any pores to conclude whether the fracture mechanism of PM metals becomes congruent with that of wrought metals.

Acknowledgements

Synchrotron radiation experiments were performed at the BL20XU beamline of SPring-8 with the approval of Japan Synchrotron Radiation Research Institute (JASRI) (Proposal No. 2018B1263). This work was also partially supported by I^2CNER at Kyusyu University. We thank JFE Steel Co. for preparing the sintered specimens. We are grateful to Professors Masato Niibe, Hiroki Adachi, and Hiroyuki Toda for their assistance with our work at SPring-8. We are also grateful to Professor Tomoyuki Shirai for the helpful discussions on PH analysis. We thank Dr. Ippei Obayashi and Professor Yasuaki Hiraoka at the Center for

Advanced Intelligence Project (AIP) in RIKEN for providing the free software “HomCloud” and their appropriate advice. We would like to thank Editage (www.editage.com) for English language editing.

Funding: This work was supported in joint research with JFE Steel Corporation.

Declarations of interest: None.

Data Availability Statement:

The raw/processed data required to reproduce these findings cannot be shared at this time due to legal or ethical reasons.

References

[1] P.K. Jones, K. Buckley-Golder, H. David, R. Lawcock, D. Sarafinchan, R. Shivanath, L. Yao, Fatigue properties of advanced high density powder metal alloy steels for high performance powertrain applications, Proc. 1998 PM World Cong., Granada, Spain, EPMA, Shrewsbury, UK, 3 (1998) 150-166.

[2] H.G. Rutz, F.G. Hanejko, High density processing of high performance ferrous materials, Adv. Powder Metall. Part. Mater. 5 (1994) 117-140.

[3] T. Hayasaka, Development of high-strength PM machine parts, J. Jap. Soc. Powder Metal. 33 (1986) 1-10.

[4] H. Danninger, D. Spoljaric, G. Jangg, B. Weiss, R. Stickler, Characterization of Pressed and Sintered Ferrous Materials by Quantitative Fractography, Pract. Metallogr. 31 (1994)56-69.

[5] H. Danninger, D. Spoljaric, B. Weiss, Microstructural features limiting the performance of P/M steels, Int. J. Powder Metall. 33 (1997) 43-53.

[6] H. Danninger, B. Weiss, The influence of defects on high cycle fatigue of metallic materials, J. Mater. Process. Technol. 143-144(2003) 179-184.

[7] M. Slesar, E. Dudrová, E. Rudnayova, Plain porosity as a microstructural characteristic of sintered materials, Powder Metall. Int. 24 (1992) 232-236.

[8] J.M. Torralba, L. Esteban, E. Bernardo, M. Campos, Understanding contribution of microstructure to fracture behavior of sintered steels, Powder Metall. 57 (2014) 357.

[9] E. Dudrová, M. Kabatová, Fractography of sintered iron and steels, Powder Metall. Prog., 8 (2008) 59-75.

[10] E. Dudrová, M. Kabátová, A review of failure of sintered steels: fractography of static and dynamic crack nucleation, coalescence, growth and propagation, Powder Metall. 59 (2016) 148-167.

[11] P.F. Thomason, A theory of ductile fracture by internal necking of cavities, J. Inst. Met. 96 (1968) 360-365.

[12] F.A. McClintock, A criteria for ductile fracture by the growth of holes, J. Appl. Mech. 35(1968) 363-371.

[13] T.B. Cox, J.R. Low, An investigation of the plastic fracture of AISI 4340 and 18 nickel--200 grade maraging steels, Metall. Trans. 5 (1974) 1457-1470.

[14] H. Toda, I. Sinclair, J.-Y. Buffiere, E. Maire, T. Connolley, M. Joyce, K.H. Khor, P. Gregson, Assessment of the fatigue crack closure phenomenon in damage-tolerant aluminum alloy by in-situ high-resolution synchrotron X-ray microtomography, Phil. Mag. A. 83 (2003) 2429-2448.

[15] H. Toda, I. Sinclair, J.-Y. Buffiere, E. Maire, K.H. Khor, P. Gregson, T. Kobayashi, A 3D measurement procedure for internal local crack driving forces via synchrotron X-ray microtomography, Acta Mater. 52 (2004) 1305-1317.

[16] L. Qian, H. Toda, K. Uesugi, T. Kobayashi, T. Ohgaki, M. Kobayashi, Application of synchrotron x-ray microtomography to investigate ductile fracture in Al alloys, Appl. Phys. Lett. 87 (2005) 241907-1-241907-1-3.

[17] T. Ohgaki, H. Toda, M. Kobayashi, K. Uesugi, M. Niinomi, T. Akahori, T. Kobayashi, K. Makii, Y. Aruga, In situ observations of compressive behaviour of aluminium foams by local tomography using high-resolution X-rays, Philos. Mag. A 86 (2006) 4417-4438.

[18] H. Toda, K. Uesugi, A. Takeuchi, K. Minami, M. Kobayashi, T. Kobayashi, Three-dimensional observation of nanoscopic precipitates in an aluminum alloy by microtomography with Fresnel zone plate optics, Appl. Phys. Lett. 89 (2006) 143112-1-143112-3.

[19] M. Kobayashi, H. Toda, K. Uesugi, T. Ohgaki, Kobayashi, Y. Takayama, B.-G. Ahn, Preferential penetration path of gallium into grain boundary in practical aluminium alloy,

Phil. Mag. A 86 (2006) 4351-4366.

[20] O. Furukimi, Y. Takeda, M. Yamamoto, M. Aramaki, S. Munetoh, A. Takeuchi, H. Ide, M. Nakasaki, Voids nucleation and growth examination during tensile deformation for IF steel by synchrotron X-ray laminography and EBSD, Tetsu-to-Hagane, 103 (2017) 475-482.

[21] N. Chawla, S. J. Polasik, K. S. Narasimhan, T.Murphy, M. Koopman, K.K. Chawla, Fatigue behavior of binder-treated P/M steels, Int. J. Powder Metall., 37(2001)49-57.

[22] S. J. Polasik, J.J. Williams, N. Chawla, Fatigue crack initiation and propagation of binder-treated powder metallurgy steels, Metall. Mater. Trans. A, 33 (2002) 73-81.

[23] N. Chawla, X. Deng, Microstructure and Mechanical Behavior of Porous Sintered Steels, Mater. Sci. Eng. A, 390 (2005) 98-112.

[24] N. Chawla, J.J. Williams, X. Deng, C. McClimon, L. Hunter, S.H. Lau, Three-dimensional characterization and modeling of porosity in PM steels, Int. J. Powder Metall. 45 (2009) 19-27.

[25] Y. Ozaki, Y. Mugita, M. Aramaki, O. Furukimi, S. Oue, F.Jiang, T.Tsuji, A. Takeuchi, M. Uesugi, K. Ashizuk, Four-dimensional observation of ductile fracture in sintered iron using synchrotron X-ray laminography, Powder Metall. 62 (2019) 146-154.

[26] S. Gondrom, J. Zhou, M. Maisl, H. Reiter, M. Kröning, W. Arnold, X-ray computed laminography: an approach of computed tomography for applications with limited access, Nucl. Eng. Des. 190 (1999) 141-147.

[27] L. Helfen, T. Baumbach, P. Mikulík, D. Kiel, P. Pernot, P. Cloetens, J. Baruchel, High-resolution three-dimensional imaging of flat objects by synchrotron-radiation computed laminography, Appl. Phys. Lett. 86 (2005) 071915-1-071915-3.

[28] M. Hoshino, K. Uesugi, A. Takeuchi, Y. Suzuki, N. Yagi, Development of an X-ray Micro-Laminography System at SPring-8, AIP Conf. Proc. 1365 (2011) 250-253.

[29] I. Obayashi, Volume-Optimal Cycle: Tightest Representative Cycle of a Generator in

Persistent Homology, SIAM J. Appl. Algebra Geometry, 2 (2018) 508-534.

[30] HomCloud. https://homcloud.dev/index.html.

Declaration of interests

☒ The authors declare that they have no known competing financial interests or personal relationships that could have appeared to influence the work reported in this paper.

Credit Author Statement

Isshin Ando: Methodology, Formal analysis, Investigation and Visualization

Yasutaka Mugita: Formal analysis, Investigation and Visualization,

Kyosuke Hirayama: Resources and Investigation

Shinji Munetoh: Formal analysis

Masatoshi Aramaki: Validation

Fei Jiang: Methodology and Writing - Review & Editing

Takeshi Tsuji: Methodology and Writing - Review & Editing

Akihisa Takeuch: Methodology, Validation and Writing - Review & Editing

Masayuki Uesugi: Methodology, Validation and Resources

Yukiko Ozaki: Conceptualization, Validation, Writing - Original Draft, Project administration and Funding acquisition.